Rotation symmetry breaking in the normal state of a kagome superconductor KV_3Sb_5

Hong Li[1,7], He Zhao[1,7], Brenden R. Ortiz[2,3], Takamori Park[4], Mengxing Ye[5], Leon Balents[5,6], Ziqiang Wang[1], Stephen D. Wilson[2,3] and Ilija Zeljkovic[1]✉

Recently discovered superconductors AV_3Sb_5 (A = K, Rb, Cs)[1,2] provide a fresh opportunity to study correlation-driven electronic phenomena on a kagome lattice. The observation of an unusual charge density wave (CDW) in the normal state of all the members of the AV_3Sb_5 family[2–10] has prompted a large effort to identify any 'hidden' broken symmetries associated with it. We use spectroscopic-imaging scanning tunnelling microscopy to reveal pronounced intensity anisotropy between the different directions of hexagonal CDW in KV_3Sb_5. In particular, we find that one of the CDW directions is distinctly different compared with the other two. This observation points to an intrinsic rotation-symmetry-broken electronic ground state where the symmetry is reduced from sixfold to twofold. Furthermore, in contrast to previous reports[3], we find that the CDW phase is insensitive to the magnetic-field direction, regardless of the presence or absence of atomic defects. Our experiments, combined with earlier observations of stripe charge ordering in CsV_3Sb_5, establish correlation-driven rotation symmetry breaking as a unifying feature of AV_3Sb_5 kagome superconductors.

Quantum materials built from atoms arranged on a kagome network are predicted to exhibit unconventional electronic behaviour[11–15] due to non-trivial Berry phase effects and strong electronic interactions. Experimental efforts on this front have primarily focused on transition-metal kagome magnets[16–20], in pursuit of realizing exotic phenomena such as topological flat bands, Weyl nodes and tunable Dirac fermions. Distinct from magnetically ordered kagome systems, recently discovered kagome metals such as AV_3Sb_5 (A = K, Rb, Cs)[1] do not exhibit a resolvable magnetic order[1,2,21]. Surprisingly, however, they show a large unconventional anomalous Hall response[7,22]. Furthermore, resembling the phenomena observed in high-temperature superconductors, AV_3Sb_5 also exhibit various density wave phases[2–10] and superconductivity[2,4–6,9,23,24], including a unidirectional $4a_0$ charge order[4,6] (where a_0 is the lattice constant) and the potential emergence of a Cooper-pair density wave[6] in CsV_3Sb_5.

Aside from superconductivity, a common feature identified across all the members of this kagome family is a $2a_0 \times 2a_0$ charge density wave (CDW) that develops in the normal state above the superconducting transition (CDW temperature onset $T_{CDW} \approx 80\text{–}100\,\text{K}$)[2,8,23]. This CDW phase has attracted much experimental[2–10,25] and theoretical[26–32] interest, as it is the first symmetry-broken phase that emerges on cooling the system down from room temperature. As such, other phases that form at lower temperatures develop from

this symmetry-broken state, and may carry the fingerprint of the $2a_0$ CDW phase. The majority of theoretical proposals and experiments to date have focused on modelling and understanding $2a_0 \times 2a_0$ CDW as an electronic phase where the three CDW directions are identical (3Q-CDW). In this work, using spectroscopic-imaging scanning tunnelling microscopy (STM), we reveal an intrinsic rotation symmetry breaking in the $2a_0 \times 2a_0$ CDW phase of KV_3Sb_5. By exploring the amplitude of CDW peaks in the Fourier transforms (FTs) of STM differential conductance maps as a function of energy, we find that one of the CDW directions is different than the other two, which reduces the rotation symmetry from C_6 to C_2. By imaging the same area of the sample with the same STM tip in different magnetic fields, we reveal that this directionality is not sensitive to the magnitude or direction of the magnetic field, which is in contrast to a recent report on an unconventional CDW tunable by a magnetic field in KV_3Sb_5 (ref. [3]). Our work establishes a unifying picture of rotation symmetry breaking as a generic feature of AV_3Sb_5 kagome superconductors.

KV_3Sb_5 is a layered kagome superconductor (superconducting transition temperature $T_c \approx 0.9\,\text{K}$) characterized by a hexagonal crystal structure ($a = b = 5.4\,\text{Å}$ and $c = 9\,\text{Å}$)[23] composed of alternately stacked V–Sb slabs and K layers (Fig. 1a,b). Each V–Sb slab can be described by a kagome lattice of V atoms interweaved by a hexagonal lattice of Sb atoms. Consistent with previous works[3–6], we find that the sample cleaves between the alkali (K) layer and Sb layer. This exposes either a K surface often prone to reconstruction (Extended Data Fig. 1) or a complete Sb surface (which we focus on in this work). STM topographs of the Sb layer show a honeycomb-like surface structure (Fig. 1c). To visualize the large-scale electronic band structure, we use quasiparticle interference imaging. This method relies on the detection of elastic scattering and interference of electrons as static, periodic charge modulations in differential conductance $dI/dV(\mathbf{r}, V)$ maps. In our sample, FTs of the $dI/dV(\mathbf{r}, V)$ maps show an isotropic scattering vector $\mathbf{q}_1$ near the FT centre in the momentum-transfer space ($\mathbf{q}$ space) (Fig. 2a,b). Similar to the spectroscopic mapping of the Sb surface of CsV_3Sb_5 (ref. [4]), $\mathbf{q}_1$ can be observed across a wide range of energies. Its magnitude and dispersion are consistent with an electron-like band at the centre of the Brillouin zone, primarily associated with the Sb orbitals (Fig. 2c). The Fermi vector $\mathbf{k}_f \approx 0.18\,\text{Å}^{-1}$ determined from our data ($\mathbf{q}_1(E=0) = 2\mathbf{k}_f$) also shows a close match to that measured by angle-resolved photoemission spectroscopy[22] and expected from calculations[23], thus demonstrating an approximate consistency between theory and different measurement techniques.

[1]Department of Physics, Boston College, Chestnut Hill, MA, USA. [2]Materials Department, University of California Santa Barbara, Santa Barbara, CA, USA. [3]California Nanosystems Institute, University of California Santa Barbara, Santa Barbara, CA, USA. [4]Department of Physics, University of California Santa Barbara, Santa Barbara, CA, USA. [5]Kavli Institute for Theoretical Physics, University of California Santa Barbara, Santa Barbara, CA, USA. [6]Canadian Institute for Advanced Research, Toronto, Canada. [7]These authors contributed equally: Hong Li, He Zhao. ✉e-mail: ilija.zeljkovic@bc.edu
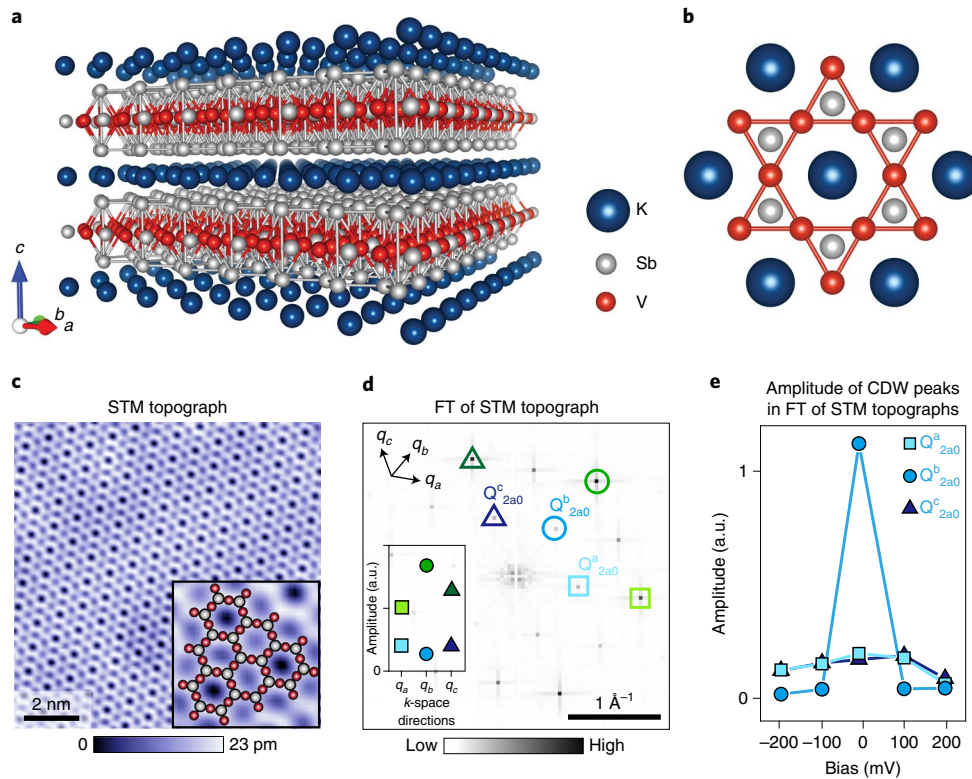
Fig. 1 | Crystal structure of KV$_3$Sb$_5$ and surface morphology. a, Three-dimensional crystal structure of KV$_3$Sb$_5$ depicting two layers, each with a thickness of one unit cell, stacked on top of one another. **b**, Atomic structure of different a–b planes superimposed on top of one another: triangular K layer, hexagonal Sb layer and kagome V–Sb slab. **c,d**, STM topograph of a square region (approximately 11 nm) of the Sb surface (**c**) and its associated FT (**d**). The inset in **c** shows a zoomed-in view of a small region of the topograph, portraying the variation in $2a_0$ intensity with the V–Sb kagome layer superimposed on top. The three different CDW peaks and atomic Bragg peaks are enclosed by shapes of different colours. The inset in **d** shows the amplitudes (peak heights) of the atomic Bragg peaks and CDW peaks in the topograph in **d**. **e**, Amplitudes of the three CDW peaks in the FTs of five different STM topographs acquired over the same area of the sample with the same STM tip. STM setup conditions: current setpoint $I_{set} = 400$ pA, sample bias $V_{sample} = 40$ mV (**c**). $I_{set} = 400$ pA, $V_{sample} = 200$ mV; $I_{set} = 200$ pA, $V_{sample} = 100$ mV; $I_{set} = 60$ pA, $V_{sample} = -10$ mV; $I_{set} = 200$ pA, $V_{sample} = -100$ mV; $I_{set} = 400$ pA, $V_{sample} = -200$ mV (**e**). The magnetic field (B) is set to 0 T. The data were acquired on sample A using tip 1.

In addition to the hexagonal lattice, STM topographs also reveal periodic conductance variations between neighbouring unit cells (Fig. 1c,d). This is consistent with the established $2a_0 \times 2a_0$ CDW phase of AV$_3$Sb$_5$ (refs. [2–9]), with momentum-space ordering wave vectors $\mathbf{Q}^i_{2a_0} = \frac{1}{2}\mathbf{Q}^i_{Bragg}$ ($i = a$, b, c) that can be clearly seen in the FT of an STM topograph (Fig. 1d). We note that the FT peak corresponding to a $4a_0$ charge-ordering peak observed in CsV$_3$Sb$_5$ (refs. [4,6]) is absent in KV$_3$Sb$_5$ (Fig. 1d). To demonstrate the CDW origin of $\mathbf{Q}^i_{2a_0}$ peaks, as opposed to energy-dispersive quasiparticle interference features, we point that these peaks do not disperse in the FTs of dI/dV($\mathbf{r}$,V) maps as a function of bias (Fig. 2d). We note that we apply the Lawler–Fujita drift-correction algorithm[33] to all our data to align the atomic Bragg peaks onto single pixels with coordinates that are even integers (defined with respect to the centre of the FT). This processing method, in turn, confines the CDW FT peaks $\mathbf{Q}^i_{2a_0} = \frac{1}{2}\mathbf{Q}^i_{Bragg}$ ($i = a$, b, c) to a single pixel, which enables an easy readout and comparison of the CDW amplitudes at different wave vectors and across different datasets. This process also minimizes the smearing of FT peaks across neighbouring pixels due to a small piezoelectric drift and thermal effects. Our first observation is that different CDW peaks display a small difference in amplitude (peak height), as shown in Fig. 1d. Moreover, the relative amplitude between the different peaks depends on the imaging bias, and the anisotropy between different directions becomes very pronounced near the Fermi level (Fig. 1e). Although the STM tips are typically

somewhat anisotropic, we point out that the amplitude of the strongest atomic Bragg peak $\mathbf{Q}^b_{Bragg}$ actually corresponds to the weakest CDW peak $\mathbf{Q}^b_{2a_0}$ (Fig. 1d, inset). As we will demonstrate below, this directionality is not a trivial consequence of STM tip anisotropy and it is rooted in the underlying rotation symmetry breaking of the electronic structure.

To explore this further, we track the evolution of the CDW peak amplitudes in the FTs of dI/dV($\mathbf{r}$,V) maps (Fig. 3a–c). For a conventional 3Q-CDW phase, the three CDW directions $\mathbf{Q}^i_{2a_0}$ should be equivalent; as such, the amplitudes at the corresponding FT wave vectors should, in principle, follow the same energy dependence. In contrast to this, we find that the peak amplitude along one of the CDW directions exhibits a markedly different energy dependence compared with the other two. For example, in Fig. 3c, we can observe that the amplitude profile associated with $\mathbf{Q}^a_{2a_0}$ and $\mathbf{Q}^c_{2a_0}$ is nearly identical, but the one related to $\mathbf{Q}^b_{2a_0}$ is noticeably different. This results in pronounced unidirectionality in dI/dV($\mathbf{r}$,V) maps that can also be observed in real space (Fig. 3d). The slight difference between the two equivalent peaks, namely, $\mathbf{Q}^a_{2a_0}$ and $\mathbf{Q}^c_{2a_0}$, may be related to a small tip anisotropy (Fig. 3c). We rule out tip artifacts in producing the apparent C_2 symmetry in the STM data by imaging the rotation of the symmetry axis across a CDW domain boundary (Fig. 3e and Extended Data Fig. 2). Our observation that one CDW peak differs from the other two is robust across multiple samples scanned with different STM tip wires (Figs. 3c and 4e and
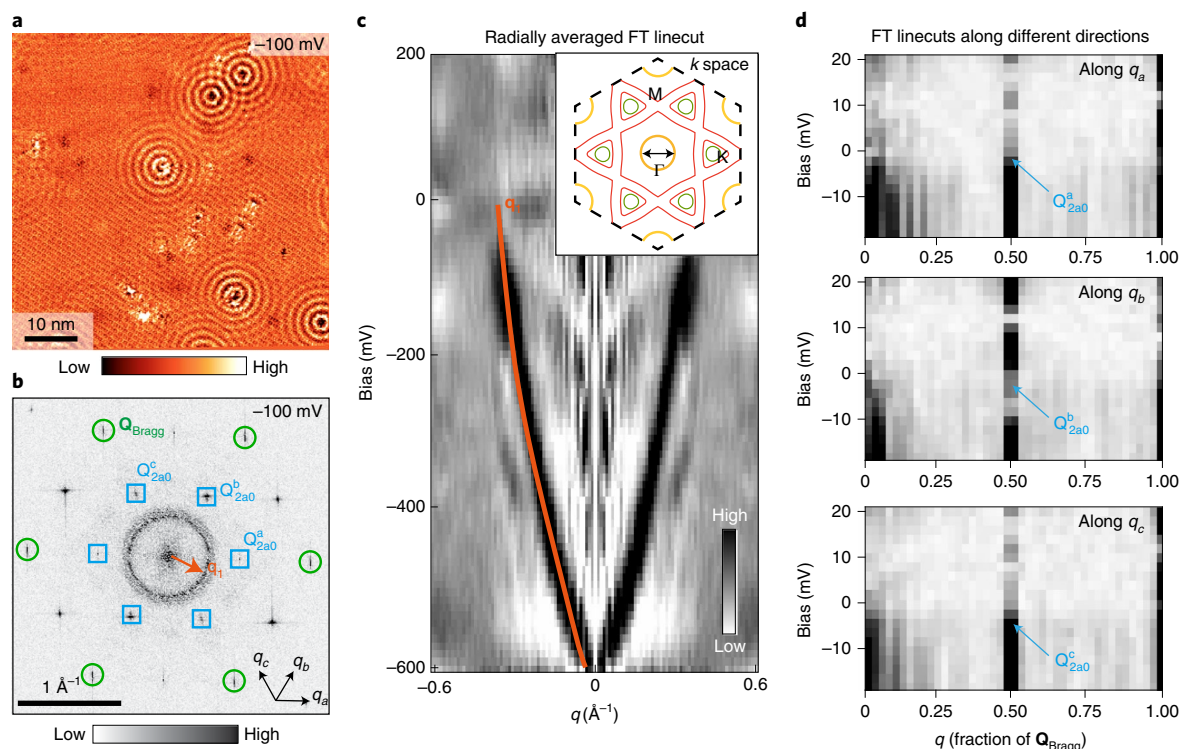
Fig. 2 | Spectroscopic-imaging scanning tunnelling microscopy of the Sb surface. a,b, Representative $dI/dV(\mathbf{r},V)$ map of approximately 60-nm-square region of the Sb termination at $-100\,$mV (**a**) and its associated FT (**b**). The prominent real-space modulations in **a** centred around impurities correspond to the reciprocal wave vector $\mathbf{q}_1$ in **b**. The green circles (blue squares) in **b** denote the atomic Bragg peaks (CDW peaks). **c,** Radially averaged linecut of FTs of normalized $dI/dV(\mathbf{r},V)/(I(\mathbf{r},V)/V)$ maps as a function of bias, acquired over the region shown in **a**. The orange line in **c** approximately denotes the dispersion of $\mathbf{q}_1$. The inset in **c** is a schematic of the Fermi surface, and the black arrow near the Γ point denotes a scattering vector related to $\mathbf{q}_1$ observed in the spectroscopic maps. **d,** FT linecuts of $dI/dV(\mathbf{r},V)$ maps along three lattice directions as a function of bias, acquired over a 12 nm area at ~4.5 K. STM setup conditions: $I_{set}=200\,$pA, $V_{sample}=-100\,$mV, bias modulation $V_{exc}=10\,$meV, $B=0\,$T (**a**); $I_{set}=900\,$pA, $V_{sample}=300\,$mV, $V_{exc}=10\,$meV, $B=0\,$T (**c**); $I_{set}=400\,$pA, $V_{sample}=20\,$mV, $V_{exc}=1\,$meV, $B=0\,$T (**d**). The data were acquired on sample A using tip 2.

Extended Data Figs. 2 and 3). We note that this is distinctly different from the CDW amplitude profiles in the prototypical CDW material $2H$-NbSe$_2$, where the amplitude profiles are comparable along all the three directions (Extended Data Fig. 4). This provides strong evidence that the electronic ground state in KV$_3$Sb$_5$ is C_2 symmetric at low temperatures.

All the experiments discussed thus far have been performed at zero external magnetic field. Given the proposals of time-reversal symmetry-breaking orbital currents[26,28] associated with the CDW phase, it is crucial to determine if and how the observed CDW signal couples to the external magnetic field[3]. To investigate this, we repeat the STM measurements as a function of magnetic field B. The relative heights of all the CDW peaks in the FTs of STM topographs appear comparable before and after a moderate external field is applied perpendicular to the c axis (Fig. 4d). Importantly, the amplitudes are insensitive to the magnetic-field direction (that is, B is applied either parallel and antiparallel to the c axis) (Fig. 4d). The robustness of CDW to reversal in the magnetic-field direction is in contrast to a recent report of a CDW order tunable by the magnetic field in the same material[3]. We note that the area shown in Fig. 4 does not contain defects that are occasionally seen in Fig. 2a; therefore, defect pinning may not explain the contrasting observations, as hypothesized elsewhere[3]. The observations reported here are confirmed in bias-dependent $dI/dV(\mathbf{r},V)$ maps of defect-free regions (Fig. 4e) and the STM topographs of multiple samples (Extended Data Fig. 5). We also note that the relative amplitudes of CDW-ordering wave vectors do not change with magnetic-field reversal in the cousin compound CsV$_3$Sb$_5$ (Extended Data Fig. 6).

Our experiments reveal a pronounced rotation symmetry breaking in the $2a_0\times2a_0$ CDW phase of KV$_3$Sb$_5$, with a single reflection symmetry preserved along the dominant CDW direction (Figs. 3c and 4e and Extended Data Figs. 2 and 3). Given the reports of unidirectional CDWs[4] and anisotropic transport measurements[34,35] in CsV$_3$Sb$_5$, which clearly break the rotation symmetry of the lattice, our measurements establish rotation symmetry breaking as a unifying feature of this family of kagome superconductors. Removing the randomly oriented CDW domains (Fig. 3e)—possibly by uniaxial stress—may facilitate the detection of electronic anisotropy by non-local probes. The observation of distinct spatial patterns across a CDW domain boundary that cannot be explained only by a simple rotation of the symmetry axis and different CDW intensity profiles on different samples (Extended Data Fig. 2 and Methods) hint that multiple C_2-symmetric charge-ordering configurations may be realized in KV$_3$Sb$_5$. Emergent theoretical evidence suggests several different possibilities for rotation symmetry breaking in the $2a_0\times2a_0$ CDW state[29,30,32]. Coupling between adjacent kagome planes stacked along the c axis with an in-plane phase offset would naturally give rise to a preferred direction seen in experiments[30,32]. This can be achieved by the condensation of the CDW order parameter connecting different points within the Brillouin zone (M and/or L points)[32]. Additionally, a complex CDW ground state within an individual kagome plane can also be at play[29]. A complete quantitative understanding of the balance between these symmetry-breaking channels and the relation to the observed CDW amplitude profile will require more detailed theoretical modelling and a comprehensive comparison with experimental data, which is beyond the scope
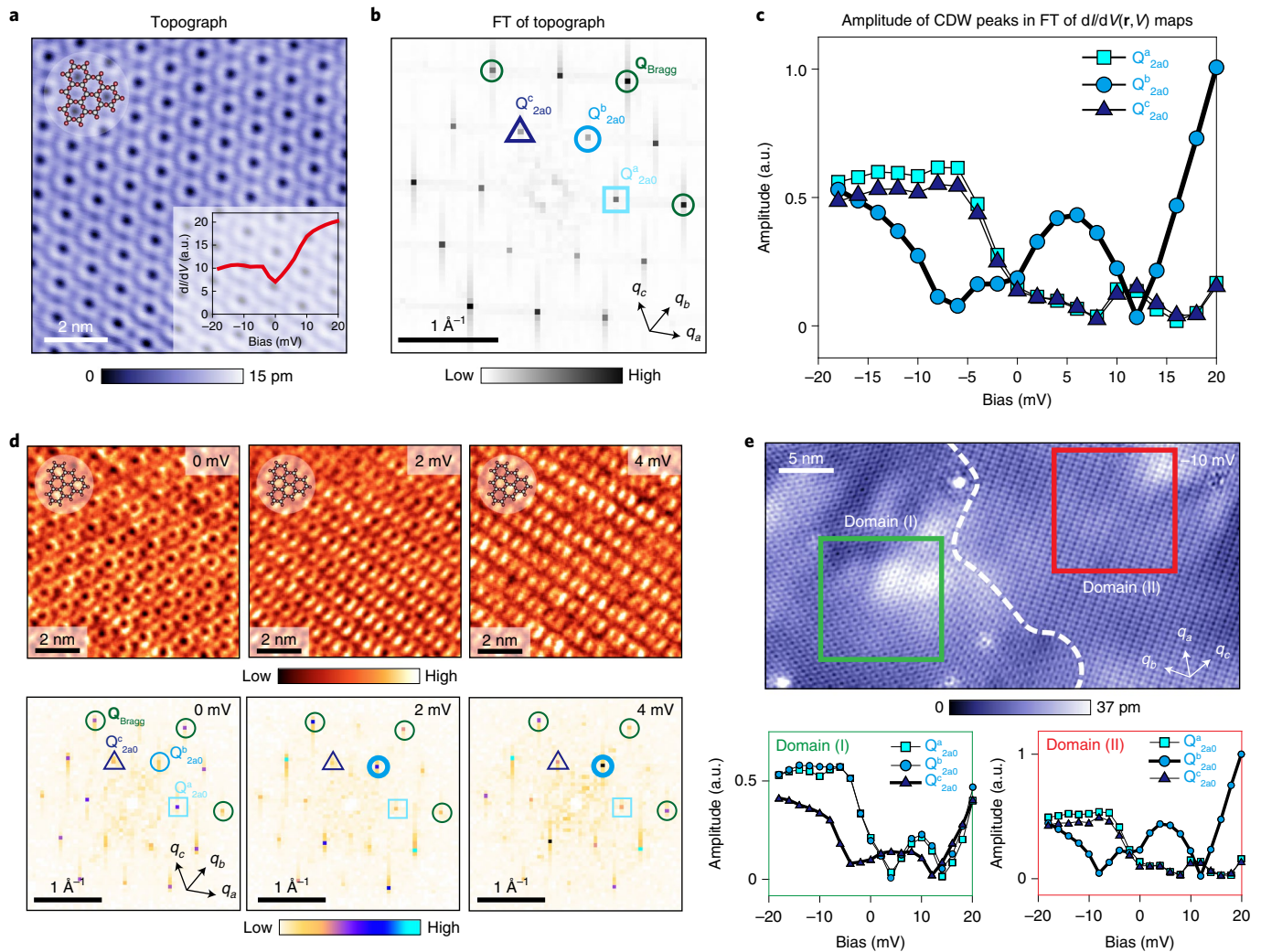
Fig. 3 | Anisotropy between inequivalent CDW directions and its atomic-scale signature in spectroscopic maps. a,b, STM topograph of approximately 10-nm-square Sb surface (**a**) and its associated FT (**b**). A layout of the V–Sb atomic structure is marked in the top-left corner of **a** (V is denoted by red spheres and Sb, by grey spheres). The bottom-right inset in **a** is the average dI/dV spectrum. **c,** Amplitude of different CDW peaks in the FTs of $dI/dV(\mathbf{r},V)$ maps as a function of STM bias V. While the dispersion of $\mathbf{Q}_{2a_0}^a$ and $\mathbf{Q}_{2a_0}^c$ is nearly identical, the dispersion of $\mathbf{Q}_{2a_0}^b$ is markedly different. **d,** High-resolution $dI/dV(\mathbf{r},V)$ maps at 0, 2 and 4 mV over the region in **a** (top row) and their associated FTs (bottom row). The three CDW peaks are enclosed by triangle, circle and square markers in all the panels, using different shades of blue. **e,** STM topograph over a domain boundary (top row) and CDW amplitude profiles along the three directions associated with two domains: domain (I) (green square in the STM topograph) and domain (II) (red square). STM setup conditions: $I_{set}=500\,pA$, $V_{sample}=40\,mV$, $B=0\,T$ (**a**); $I_{set}=400\,pA$, $V_{sample}=20\,mV$, $V_{exc}=1\,meV$, $B=0\,T$ (**c**); $I_{set}=150\,pA$, $V_{sample}=10\,mV$, $V_{exc}=1\,meV$, $B=0\,T$ (**d**); $I_{set}=120\,pA$, $V_{sample}=-10\,mV$ (**e**). The data were acquired on sample A using tip 3.

of the current work. Nevertheless, our experiments provide strong evidence that the structure of the CDW in this system goes beyond the simple, rotationally symmetric state with either 'Star-of-David' or inverse Star-of-David morphology[27].

Despite a close resemblance between the electronic band structures of KV_3Sb_5 and CsV_3Sb_5, an intriguing difference between the two systems is that KV_3Sb_5 does not show the $4a_0$ charge ordering. It may be possible that small differences in the chemical potential between the two materials play a larger role, and that the $4a_0$ charge order vanishes with doping, analogous to the $4a_0$ order in cuprates[36]. Our work suggests that superconductivity in this system emerges from a state where rotational symmetry is already broken, which should be important for developing a theoretical understanding of superconductivity in this material. Our experiments also provide a foundation to explore how the observed spatial symmetry breaking could affect the topological surface states[37].

Contrasting observations reported here and those in ref. [3] regarding the dependence of CDW on external magnetic field pose an intriguing question regarding the dichotomy of the results. We note that subtle changes in the STM tip can dramatically change the apparent CDW amplitudes (Extended Data Fig. 7). By ruling out these trivial measurement artifacts leading to the substantial CDW amplitude change, it may be conceivable that small chemical-potential variations between the different areas of nominally the same crystals could explain the discrepant results. However, based on our experiments that show the absence of CDW tunability by field direction in all the samples and crystals where measurements were performed, we can conclude that magnetic-field-based CDW tunability[3] is not a robust feature. It can perhaps be dependent on the sample area. It remains to be seen whether the time-reversal symmetry in AV_3Sb_5 is indeed broken by the orbital currents[26,28]. Future experiments using high-resolution spin-polarized STM[38] or neutron scattering[39]
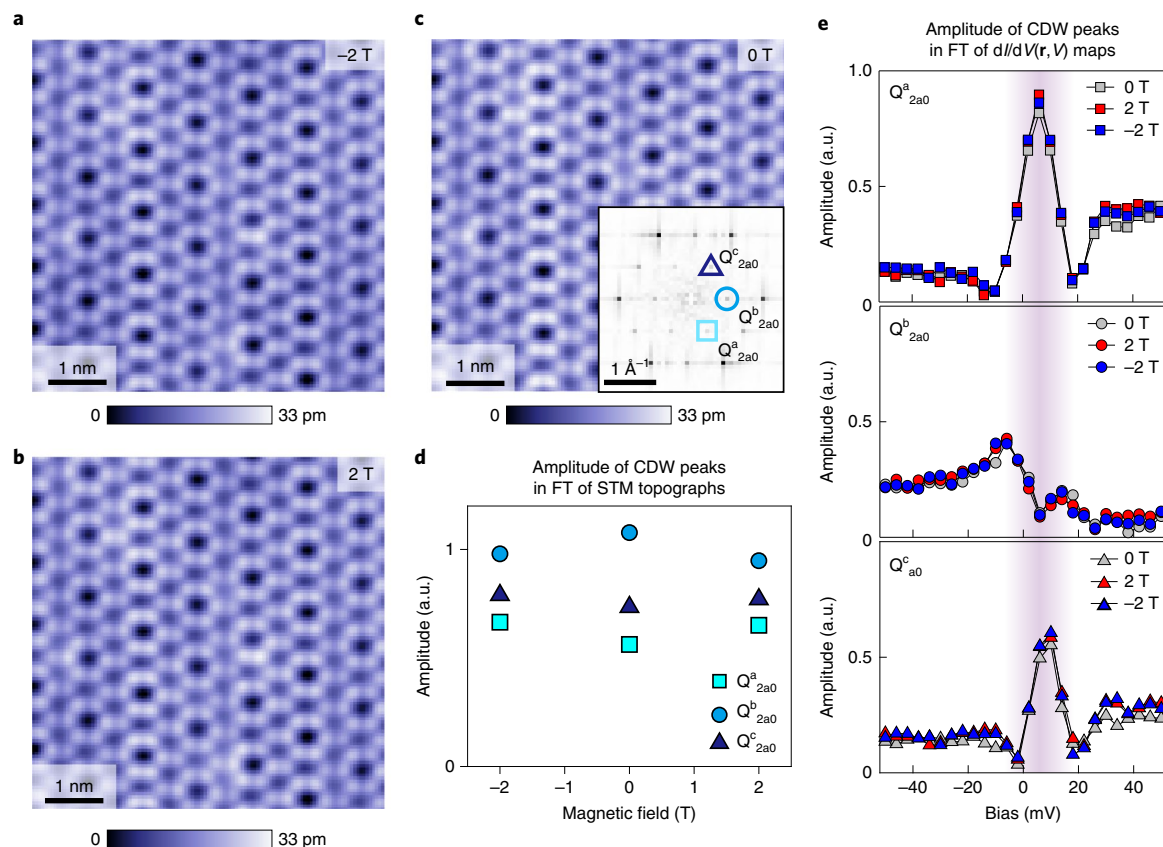
Fig. 4 | Insensitivity of CDW to external magnetic-field direction. a–c, STM topographs of an identical region of Sb surface acquired at magnetic fields of −2 T (**a**), 2 T (**b**) and 0 T (**c**). The inset in **c** shows the FTs of the topograph in **c**, with the three CDW peaks denoted by different symbols. **d**, Amplitudes of the three CDW peaks in the FTs of STM topographs in **a–c** acquired at different magnetic fields applied perpendicular to the sample surface. The sign associated with B denotes the reversal of the magnetic-field direction (parallel versus antiparallel to the c axis). **e**, Amplitudes of the CDW peaks in $dI/dV(\mathbf{r}, V)$ maps as a function of magnetic field and bias V, acquired over the region shown in **a–c**. The diffuse vertical purple line denotes the approximate energy range where the peak in the dispersion related to $\mathbf{Q}^a_{2a_0}$ (top) and $\mathbf{Q}^c_{2a_0}$ (bottom) coincides with the minimum in the $\mathbf{Q}^b_{2a_0}$ (middle) dispersion. STM setup conditions: $I_{set} = 100\,pA$, $V_{sample} = 50\,mV$ (**a–d**); $I_{set} = 100\,pA$, $V_{sample} = 50\,mV$, $V_{exc} = 4\,mV$ (**e**). The data were acquired on sample B using tip 4.

could potentially shed light on this issue by measuring any subtle, underlying magnetic background.

Online content

Any methods, additional references, Nature Research reporting summaries, source data, extended data, supplementary information, acknowledgements, peer review information; details of author contributions and competing interests; and statements of data and code availability are available at https://doi.org/10.1038/s41567-021-01479-7.

References

1. Ortiz, B. R. et al. New kagome prototype materials: discovery of KV₃Sb₅, RbV₃Sb₅, and CsV₃Sb₅. *Phys. Rev. Mater.* **3**, 094407 (2019).
2. Ortiz, B. R. et al. CsV₃Sb₅: a Z₂ topological kagome metal with a superconducting ground state. *Phys. Rev. Lett.* **125**, 247002 (2020).
3. Jiang, Y.-X. et al. Unconventional chiral charge order in kagome superconductor KV₃Sb₅. *Nat. Mater.* **20**, 1353–1357 (2021).
4. Zhao, H. et al. Cascade of correlated electron states in the kagome superconductor CsV₃Sb₅. *Nature* **599**, 216–221 (2021).
5. Liang, Z. et al. Three-dimensional charge density wave and surface-dependent vortex-core states in a kagome superconductor CsV₃Sb₅. *Phys. Rev. X* **11**, 031026 (2021).
6. Chen, H. et al. Roton pair density wave in a strong-coupling kagome superconductor. *Nature* **599**, 222–228 (2021).
7. Yu, F. H. et al. Concurrence of anomalous Hall effect and charge density wave in a superconducting topological kagome metal. *Phys. Rev. B* **104**, L041103 (2021).
8. Li, H. et al. Observation of unconventional charge density wave without acoustic phonon anomaly in kagome superconductors AV₃Sb₅ (A = Rb, Cs). *Phys. Rev. X* **11**, 031050 (2021).
9. Chen, K. Y. et al. Double superconducting dome and triple enhancement of T_c in the kagome superconductor CsV₃Sb₅ under high pressure. *Phys. Rev. Lett.* **126**, 247001 (2021).
10. Wang, Z. et al. Distinctive momentum dependent charge-density-wave gap observed in CsV3Sb5 superconductor with topological kagome lattice. Preprint at https://arxiv.org/abs/2104.05556 (2021).
11. Sachdev, S. Kagome- and triangular-lattice Heisenberg antiferromagnets: ordering from quantum fluctuations and quantum-disordered ground states with unconfined bosonic spinons. *Phys. Rev. B* **45**, 12377–12396 (1992).
12. Guo, H.-M. & Franz, M. Topological insulator on the kagome lattice. *Phys. Rev. B* **80**, 113102 (2009).
13. Neupert, T., Santos, L., Chamon, C. & Mudry, C. Fractional quantum Hall states at zero magnetic field. *Phys. Rev. Lett.* **106**, 236804 (2011).
14. Sun, K., Gu, Z., Katsura, H. & Das Sarma, S. Nearly flatbands with nontrivial topology. *Phys. Rev. Lett.* **106**, 236803 (2011).
15. Tang, E., Mei, J.-W. & Wen, X.-G. High-temperature fractional quantum Hall states. *Phys. Rev. Lett.* **106**, 236802 (2011).
16. Wang, Q. et al. Large intrinsic anomalous Hall effect in half-metallic ferromagnet Co₃Sn₂S₂ with magnetic Weyl fermions. *Nat. Commun.* **9**, 3681 (2018).
17. Morali, N. et al. Fermi-arc diversity on surface terminations of the magnetic Weyl semimetal Co₃Sn₂S₂. *Science* **365**, 1286–1291 (2019).
18. Liu, E. et al. Giant anomalous Hall effect in a ferromagnetic kagome-lattice semimetal. *Nat. Phys.* **14**, 1125–1131 (2018).

19. Yin, J.-X. X. et al. Giant and anisotropic many-body spin–orbit tunability in a strongly correlated kagome magnet. *Nature* **562**, 91–95 (2018).

20. Kang, M. et al. Dirac fermions and flat bands in the ideal kagome metal FeSn. *Nat. Mater.* **19**, 163–169 (2020).

21. Kenney, E. M., Ortiz, B. R., Wang, C., Wilson, S. D. & Graf, M. J. Absence of local moments in the kagome metal KV_3Sb_5 as determined by muon spin spectroscopy. *J. Phys. Condens. Matter* **33**, 235801 (2021).

22. Yang, S.-Y. et al. Giant, unconventional anomalous Hall effect in the metallic frustrated magnet candidate, KV_3Sb_5. *Sci. Adv.* **6**, eabb6003 (2020).

23. Ortiz, B. R. et al. Superconductivity in the Z_2 kagome metal KV_3Sb_5. *Phys. Rev. Mater.* **5**, 034801 (2021).

24. Zhao, C. C. et al. Nodal superconductivity and superconducting domes in the topological kagome metal CsV3Sb5. Preprint at https://arxiv.org/abs/2102.08356 (2021).

25. Ortiz, B. R. et al. Fermi surface mapping and the nature of charge-density-wave order in the kagome superconductor CsV_3Sb_5. *Phys. Rev. X* **11**, 041030 (2021).

26. Feng, X., Jiang, K., Wang, Z. & Hu, J. Chiral flux phase in the kagome superconductor AV_3Sb_5. *Sci. Bull.* **66**, 1384–1388 (2021).

27. Tan, H., Liu, Y., Wang, Z. & Yan, B. Charge density waves and electronic properties of superconducting kagome metals. *Phys. Rev. Lett.* **127**, 046401 (2021).

28. Denner, M. M., Thomale, R. & Neupert, T. Analysis of charge order in the kagome metal AV_3Sb_5 (A = K, Rb, Cs). *Phys. Rev. Lett.* **127**, 217601 (2021).

29. Lin, Y.-P. & Nandkishore, R. M. Complex charge density waves at Van Hove singularity on hexagonal lattices: Haldane-model phase diagram and potential realization in the kagome metals AV_3Sb_5 (A = K, Rb, Cs). *Phys. Rev. B* **104**, 045122 (2021).

30. Park, T., Ye, M. & Balents, L. Electronic instabilities of kagome metals: saddle points and Landau theory. *Phys. Rev. B* **104**, 035142 (2021).

31. Zhao, J., Wu, W., Wang, Y. & Yang, S. A. Electronic correlations in the normal state of the kagome superconductor KV_3Sb_5. *Phys. Rev. B* **103**, L241117 (2021).

32. Christensen, M. H., Birol, T., Andersen, B. M. & Fernandes, R. M. Theory of the charge-density wave in AV3Sb5 kagome metals. Preprint at https://arxiv.org/abs/2107.04546 (2021).

33. Lawler, M. J. et al. Intra-unit-cell electronic nematicity of the high-T_c copper-oxide pseudogap states. *Nature* **466**, 347–351 (2010).

34. Ni, S. et al. Anisotropic superconducting properties of kagome metal CsV_3Sb_5. *Chinese Phys. Lett.* **38**, 057403 (2021).

35. Xiang, Y. et al. Twofold symmetry of c-axis resistivity in topological kagome superconductor CsV_3Sb_5 with in-plane rotating magnetic field. *Nat. Commun.* **12**, 6727 (2021).

36. Mesaros, A. et al. Commensurate $4a_0$-period charge density modulations throughout the $Bi_2Sr_2CaCu_2O_{8+x}$ pseudogap regime. *Proc. Natl Acad. Sci. USA* **113**, 12661–12666 (2016).

37. Hu, Y. et al. Charge-order-assisted topological surface states and flat bands in the kagome superconductor CsV3Sb5. Preprint at https://arxiv.org/abs/2104.12725 (2021).

38. Zhao, H. et al. Atomic-scale fragmentation and collapse of antiferromagnetic order in a doped Mott insulator. *Nat. Phys.* **15**, 1267–1272 (2019).

39. Fauqué, B. et al. Magnetic order in the pseudogap phase of high-T_c superconductors. *Phys. Rev. Lett.* **96**, 197001 (2006).

Methods

STM measurements. Single crystals of KV_3Sb_5 were grown and characterized as described in more detail elsewhere[23]. We cold cleaved and studied four different KV_3Sb_5 crystals (labelled A–D), all of which qualitatively exhibited the same phenomena described in the main text. The STM data were acquired using a customized UNISOKU USM1300 microscope at approximately 4.5 K. Spectroscopic measurements were made using a standard lock-in technique with 915 Hz frequency and bias excitation, as detailed in the main text. The STM tips used (labelled 1–6) were home-made chemically etched tungsten tips, annealed in an ultrahigh vacuum to a bright orange colour before STM experiments. We apply the Lawler–Fujita drift-correction algorithm[33] to all our data to align the atomic Bragg peaks onto single pixels with coordinates that are even integers. Representative data before drift correction are shown in Extended Data Figs. 8 and 9.

Ruling out STM tip artifacts. To completely rule out the possibility of tip artifacts artificially inducing the apparent CDW anisotropy, we image a CDW domain boundary between two distinct regions labelled (I) and (II) using the same STM tip. Both regions show the 2×2 CDW (Extended Data Fig. 2). The change in CDW anisotropy between the two regions is more apparent at low bias (Extended Data Fig. 2b). Based on the CDW amplitude profiles in the two regions, we can determine the rotation of the symmetry axis (Extended Data Fig. 2d,e): $\mathbf{Q}_{2a_0}^c$ is the symmetry axis in domain (I), whereas it is $\mathbf{Q}_{2a_0}^b$ in domain (II) (Extended Data Fig. 2d,e, bold lines). For visualization purposes, we Fourier filtered the STM topograph to emphasize modulations along these two wave vectors (Extended Data Fig. 2g,h). As such, the apparent C_2 symmetry in the CDW state cannot be explained by STM tip artifacts.

We proceed to examine the morphology of the CDW pattern in the two domains more closely. In both domains (I) and (II), the CDW amplitude intensity versus bias shows two directions that are identical, but the third one is markedly different ($\mathbf{Q}_{2a_0}^c$ in domain (I) and $\mathbf{Q}_{2a_0}^b$ in domain (II)). If domain (II) was identical to domain (I) but rotated by 60°, we would expect the same CDW amplitude intensity profile shown in Extended Data Fig. 2d,e, but with each curve now associated with different indices. Instead, however, domain (II) shows two directions that have a peak near 5–10 meV (Extended Data Fig. 2d) as opposed to only one (Extended Data Fig. 2e). This difference is also reflected in the distinct spatial patterns (Extended Data Fig. 2f) that go beyond a simple rotation by 60°. This suggests that the differences between the two CDW domains go beyond a simple 60° rotation, and hint at the possibility of realizing at least two distinct C_2-symmetric states.

Data availability

 Source data are provided with this paper. All other data that support the plots within this paper and other findings of this study are available from the corresponding author upon reasonable request.

Code availability

The computer code used for data analysis is available from the corresponding author upon reasonable request.

Author contributions

STM experiments and data analysis were performed by H.L. and H.Z. B.R.O. synthesized and characterized the samples under the supervision of S.D.W. T.P., M.Y., L.B. and Z.W. provided theoretical inputs on the underlying physics and data interpretation. H.L., H.Z., S.D.W, Z.W., L.B. and I.Z. wrote the paper, with input from all the authors. I.Z. supervised the project.

Competing interests

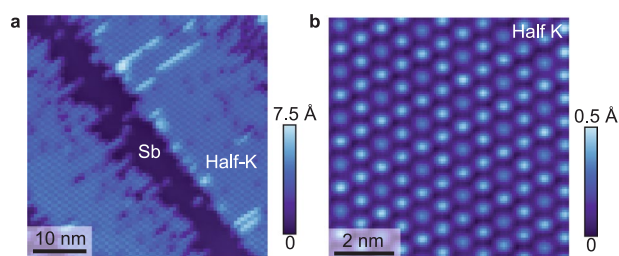The authors declare no competing interests.

Additional information

Extended data is available for this paper at https://doi.org/10.1038/s41567-021-01479-7.
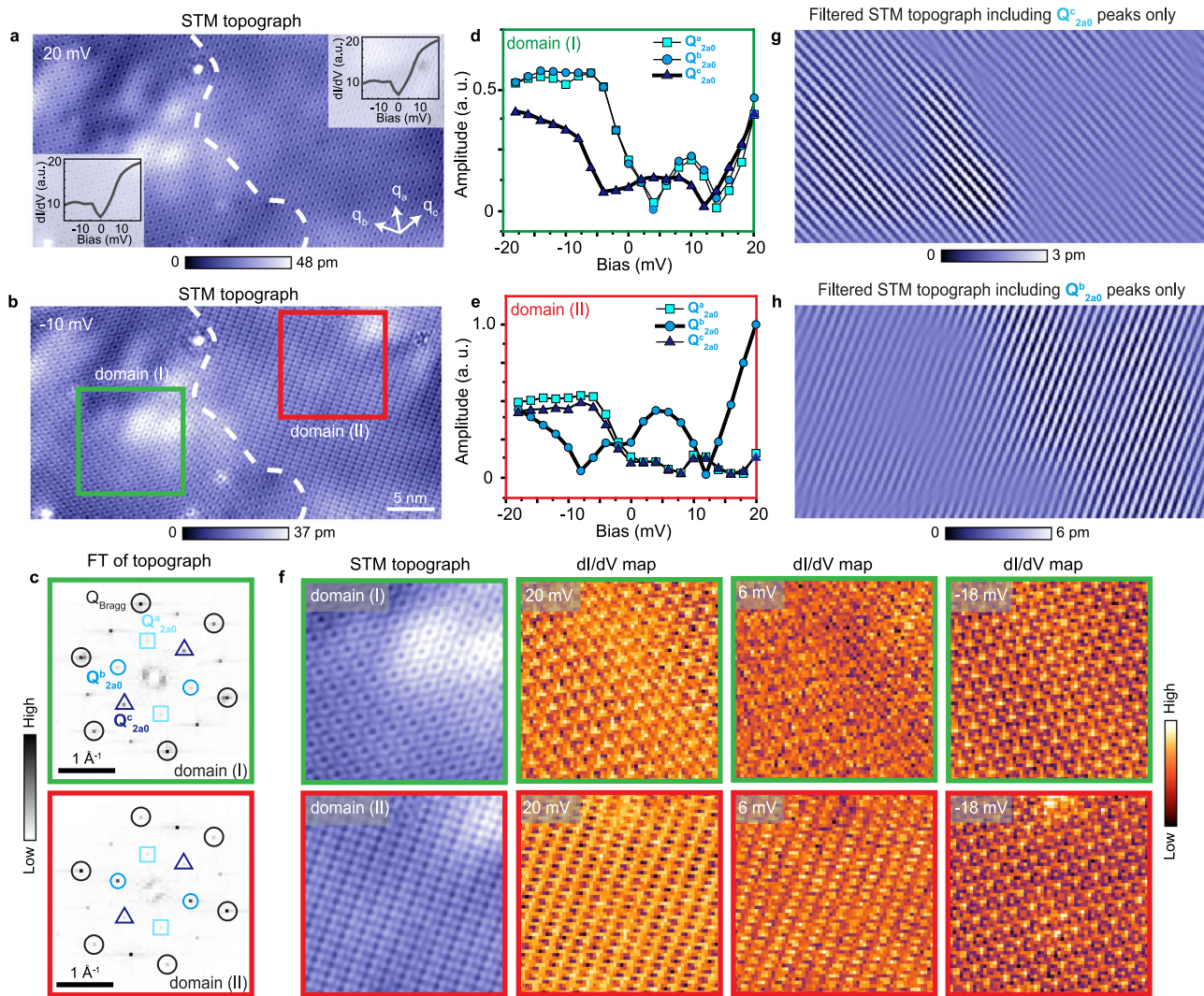
Correspondence and requests for materials should be addressed to Ilija Zeljkovic.

Peer review information *Nature Physics* thanks Donglai Feng and the other, anonymous, reviewer(s) for their contribution to the peer review of this work.
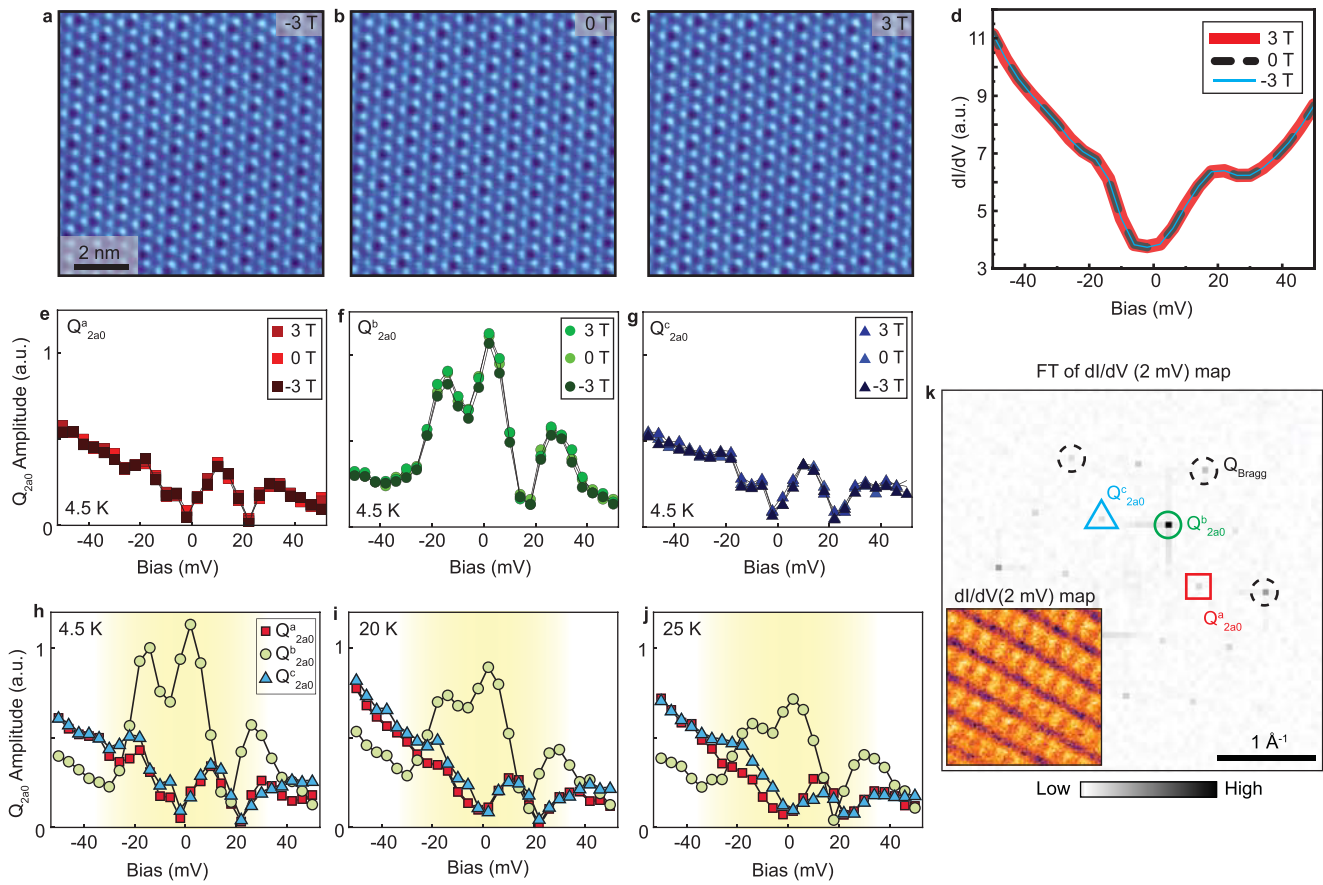
Reprints and permissions information is available at www.nature.com/reprints.
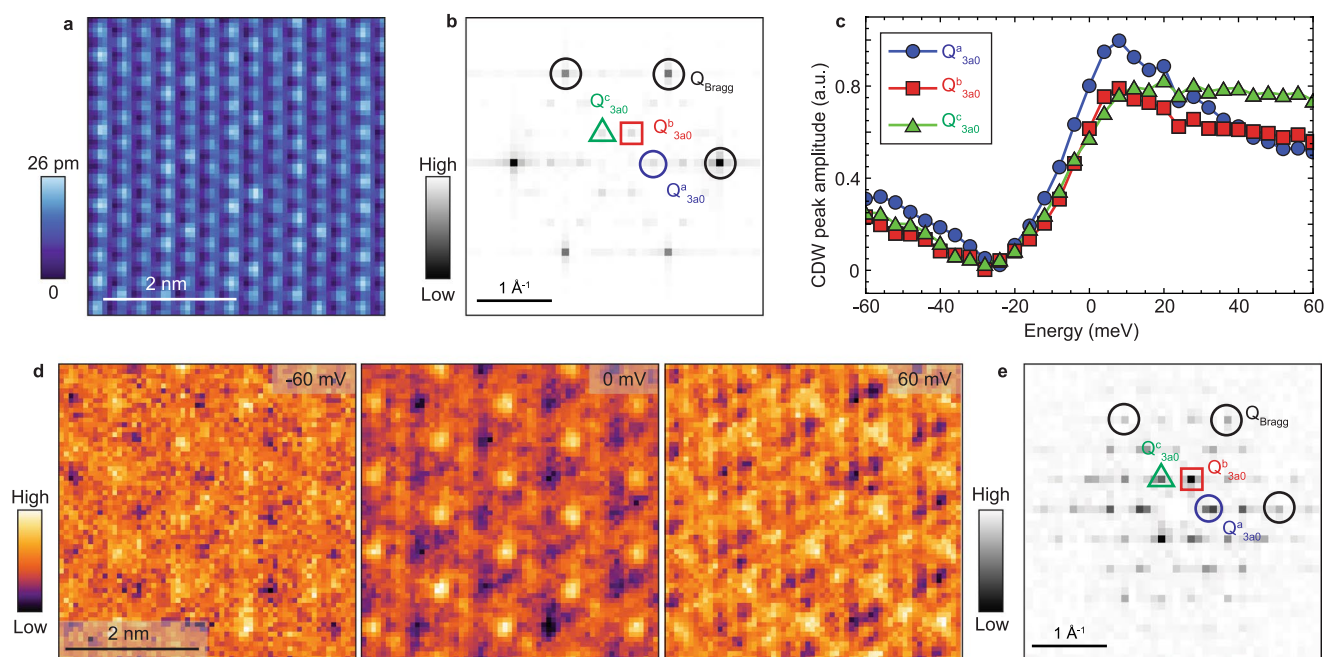
Extended Data Fig. 1 | STM topographs of the K layer. (a) Large scale STM topograph of 50 nm square region showing the half-K layer (K surface reconstruction where every other K atom is likely cleaved of) as bright regions, and the Sb layer as dark regions. (b) STM topograph zoomed in on a half-K termination with twice the lattice constant of a full K layer ($a = 1.1$ nm). STM setup condition: (a) $I_{set} = 10$ pA, $V_{sample} = 1$ V; (b) $I_{set} = 100$ pA, $V_{sample} = 20$ mV. Data was acquired on sample C with tip 5.
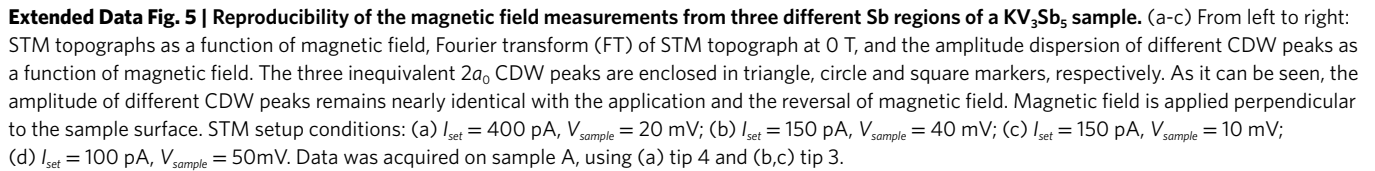
Extended Data Fig. 2 | STM imaging of a CDW domain boundary. (a,b) STM topographs of a region encompassing a CDW domain boundary taken at (a) 20 mV and (b) −10 mV. The white dashed line in (a,b) is a visual guide used to separate the two domains. A more obvious difference between the two domains can be seen in (b). Insets in upper right and lower left corners of (a) represent average dI/dV spectra over the corresponding domains. (c) Fourier transform (FT) of domain (I) and domain (II) in (f). Atomic Bragg peaks and CDW peaks are denoted by black and blue symbols, respectively. (d,e) The FT amplitude dispersions of the 3 CDW peaks extracted from the (d) green and (e) red squares in (b), demonstrating the change in the CDW symmetry axis from Q_{2a0}^c to Q_{2a0}^b across the domain wall. (f) Zoomed in image of topographs and dI/dV maps in green (upper row) and red (lower row) squares in (b). (g,h) Fourier-filtered STM topograph including only (g) Q_{2a0}^c or (h) Q_{2a0}^b Fourier peaks. STM setup conditions: (a) I_{set} = 250 pA, V_{sample} = 20 mV; (b) I_{set} = 60 pA, V_{sample} = −10 mV; (d,e) I_{set} = 400 pA, V_{sample} = 20 mV, V_{exc} = 1 mV; (f) I_{set} = 150 pA, V_{sample} = −10 mV, V_{exc} = 1 mV. Data was acquired on sample A using tip 2.
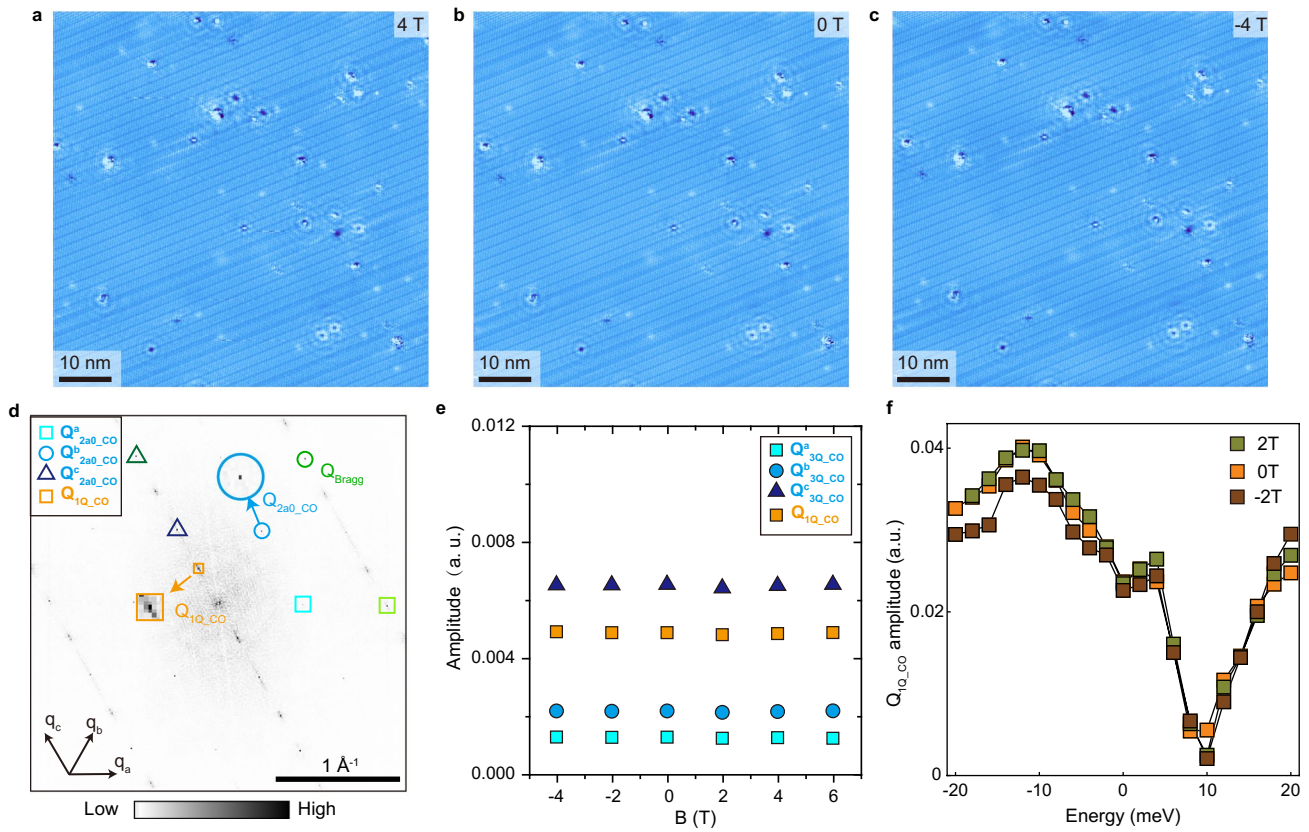
Extended Data Fig. 3 | Absence of magnetic field induced CDW reversal and visualizing the temperature evolution of the CDW in KV$_3$Sb$_5$. (a-c) STM topographs of the Sb termination taken at −3 T, 0 T and 3 T over an identical region with the same tip. (d) Average dI/dV spectra acquired over (a-c), which appear indistinguishable within the resolution of the dataset. (e-g) $2a_0$ CDW peak amplitude dispersion at the three magnetic fields for (e) Q^a_{2a0}, (f) Q^b_{2a0}, and (g) Q^c_{2a0}. There is almost no difference among data at different fields. (h-j) $2a_0$ CDW peak amplitude dispersion at 4.5 K, 20 K, and 25 K respectively over the same region of the sample, showing the dominant peak Q^b_{2a0} getting weaker at higher temperature. (k) A Fourier transform of dI/dV map acquired at 2 mV. The lower left corner of (k) is a zoomed-in high resolution dI/dV map at 2 mV. Atomic Bragg peaks are marked by black dashed circles, while Q^a_{2a0}, Q^b_{2a0}, Q^c_{2a0} are denoted by red square, green circle and blue triangle, respectively. STM setup conditions: (a-c) I_{set} = 100 pA, V_{sample} = 50 mV, (d-j) I_{set} = 100 pA, V_{sample} = 50 mV, V_{exc} = 4 mV. Data was acquired on sample D using tip 6.
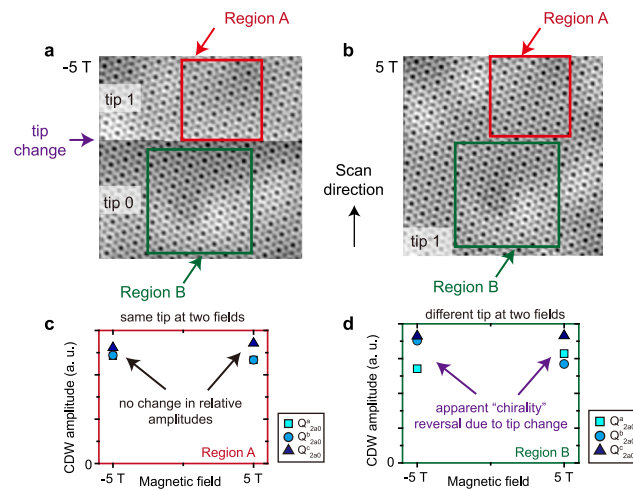
Extended Data Fig. 4 | Isotropic CDW peak dispersion in 2H- NbSe₂. (a) STM topograph of the Se surface of $2H$-NbSe$_2$ with the well-known tri-directional $3a_0$ CDW. (b) The Fourier transform (FT) of (a). Atomic Bragg peaks are circled in black, while the three inequivalent $3a_0$ CDW peaks are denoted by the blue circle, red square and green triangle. (c) CDW peak amplitude as a function of energy (STM bias) for the three inequivalent directions. Each point is obtained by a two-dimensional Gaussian fit of the CDW peak in the FTs of dI/dV maps. The CDW amplitude profiles along the three directions closely resemble each other, consistent with the expected tri-directional nature of the CDW that does not break rotation symmetry of the lattice. (d) dI/dV maps at −60 mV, 0 mV and 60 mV (from left to right) over the same region shown in (a). (e) FT of 0 mV dI/dV map in (d). Black circles denote the atomic Bragg peaks, while the blue, red and green symbols denote the three inequivalent CDW peaks. STM setup conditions: (a,c,d) I_{set} = 300 pA, V_{sample} = −60 mV, V_{exc} = 3 mV. The data was acquired in the Hoffman lab at Harvard University, and provided for analysis by Anjan Soumyanarayanan and Jenny Hoffman.
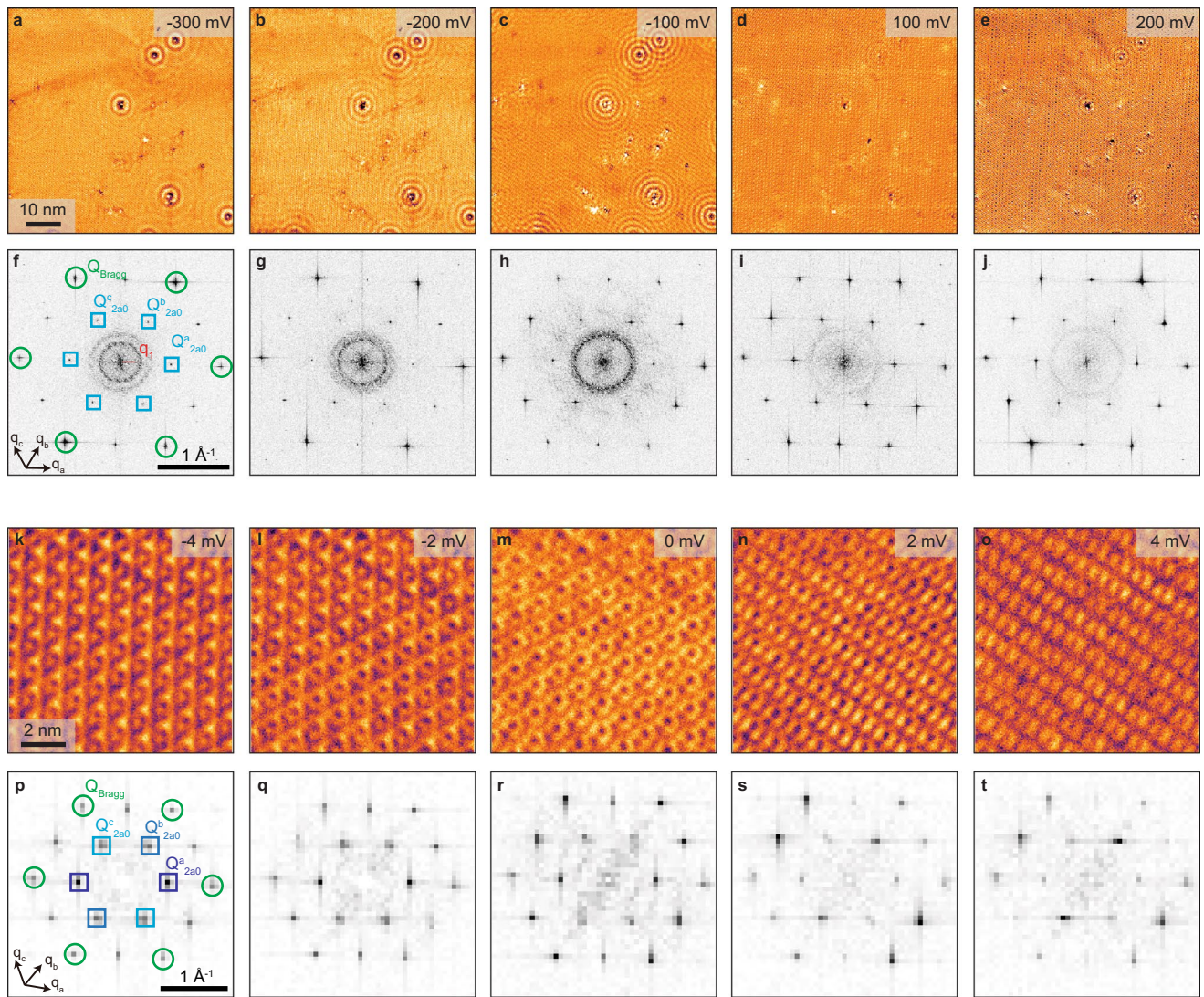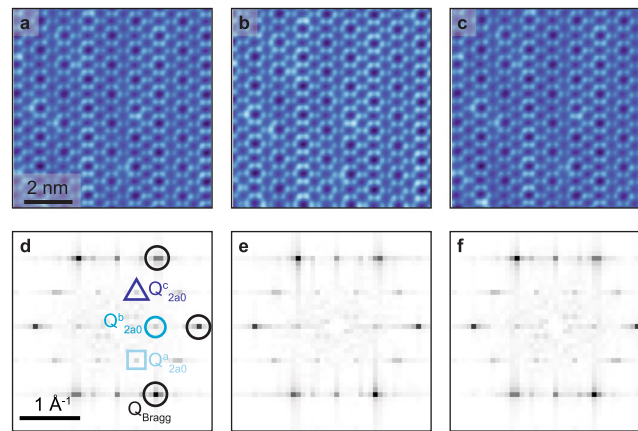
Extended Data Fig. 5 | Reproducibility of the magnetic field measurements from three different Sb regions of a KV$_3$Sb$_5$ sample. (a-c) From left to right: STM topographs as a function of magnetic field, Fourier transform (FT) of STM topograph at 0 T, and the amplitude dispersion of different CDW peaks as a function of magnetic field. The three inequivalent $2a_0$ CDW peaks are enclosed in triangle, circle and square markers, respectively. As it can be seen, the amplitude of different CDW peaks remains nearly identical with the application and the reversal of magnetic field. Magnetic field is applied perpendicular to the sample surface. STM setup conditions: (a) I_{set} = 400 pA, V_{sample} = 20 mV; (b) I_{set} = 150 pA, V_{sample} = 40 mV; (c) I_{set} = 150 pA, V_{sample} = 10 mV; (d) I_{set} = 100 pA, V_{sample} = 50mV. Data was acquired on sample A, using (a) tip 4 and (b,c) tip 3.

Extended Data Fig. 6 | Magnetic field measurements of cousin compound CsV$_3$Sb$_5$. (a-c) STM topograph of a 70 nm square Sb surface of CsV$_3$Sb$_5$ in a magnetic field of 4 T, 0 T and −4 T, respectively. Magnetic field is applied perpendicular to the sample surface. (d) The Fourier transform of STM topograph in (b). The unidirectional $4a_0$ charge ordering peak, $2a_0$ peaks and atomic Bragg peaks are marked by orange, blue and green markers, respectively. (e) Fourier transform peak amplitudes of different wave vectors. We can observe that none of the charge ordering peak intensities significantly change. (f) The amplitude of the $4a_0$ CDW peak as a function of bias extracted from a DOS map acquired over the Sb surface of the CsV$_3$Sb$_5$ sample. The 3 different colors in (f) denote data acquired in different magnetic fields. STM setup conditions: (a-c) $I_{set} = 110$ pA, $V_{sample} = -40$ mV. (f) $I_{set} = 80$ pA, $V_{sample} = 20$ mV, $V_{exc} = 1$ mV.

Extended Data Fig. 7 | An example of how a small tip change can strongly influence CDW amplitudes. (a,b) STM topographs of the Sb termination at (a) −5 T and (b) +5 T magnetic field applied along the *c*-axis. An obvious tip change occurred while scanning at −5 T. After the image in (a) was acquired, the tip was withdrawn, the magnetic field was changed to +5 T, and then the topograph in (b) over the same region of the sample was taken. We refer to the tip before the tip change as tip 0, and the one after the tip change as tip 1. The green and red squares denote the same areas in the two topographs. Red square (region A) is scanned at different field with the same tip (tip 1), while the green square (region B) is scanned with slightly different tips (tip 0 at −5 T and tip 1 at +5 T). (c,d) The plot of CDW peak amplitudes in Fourier transforms of ±5 T topographs for regions A and B, respectively. From plot (c), the relative amplitude between the 3 CDW peaks is: $Q^c_{2a0} > Q^a_{2a0} = Q^b_{2a0}$ for both +5 T and −5 T. In contrast, the relation between peaks changes dramatically in plot (d), where $Q^c_{2a0} > Q^b_{2a0} > Q^a_{2a0}$ at −5 T and $Q^c_{2a0} > Q^a_{2a0} > Q^b_{2a0}$ at +5 T. From this, it appears as if there is field-dependent CDW rotation. However, this is purely an artifact of a tiny tip change, since it did not happen in the red region above, where two topographs are taken with the same tip. We emphasize that the tip change is tiny and difficult to discern by comparing topographs by eye (we identified it by the abrupt height change denoted by purple arrow in (a)). As such, extreme caution should be taken when interpreting relative amplitudes between different data sets. STM setup conditions: (a,b) $I_{set} = 400$ pA, $V_{sample} = 40$ mV.

Extended Data Fig. 8 | Representative raw data (without drift correction). (a-e) dI/dV maps of Sb termination without drift correction taken at different bias used in Fig. 2, and (f-j) corresponding Fourier transforms (FTs). (k-o) Raw dI/dV maps that are used in Fig. 3, and (p-t) corresponding FTs without drift correction. STM setup conditions: (a-e) I_{set} = 600 pA, 400 pA, 200 pA, 200 pA and 400 pA respectively, with V_{sample}= −300 mV, −200 mV, −100 mV, 100 mV, 200 mV (in the same order); (k-o) I_{set} = 150 pA, V_{sample} = 10 mV, V_{exc} = 1 mV. Data was acquired on sample A using (a-j) tip 2 and (k-t) tip 3.

Extended Data Fig. 9 | Additional raw data (without drift correction). (a-c) Topographs used in Fig. 4, and (d-f) corresponding Fourier transforms without drift-correction. STM setup conditions: (a-c) I_{set} = 100 pA, V_{sample} = 50 mV. Data was acquired on sample B using tip 4.